

## Instruments and Methods

# Light propagation in firn: application to borehole video

T.J. FUDGE,<sup>1</sup> Benjamin E. SMITH<sup>2</sup>

<sup>1</sup>*Department of Earth and Space Sciences, University of Washington, Box 351310, Seattle, Washington 98195-1310, USA  
E-mail: tjfudge@u.washington.edu*

<sup>2</sup>*Applied Physics Laboratory, University of Washington, 1013 NE 40th Street, Box 355640, Seattle, Washington 98105-6698, USA*

**ABSTRACT.** Borehole optical stratigraphy (BOS) is a borehole video system and processing routine for investigating polar firn. BOS records brightness variations in the firn and is effective at identifying stratigraphic markers. BOS brightness logs have been used to count annual layers and measure vertical strain, even though a specific cause of the brightness variations has not been determined. Here we combine two models of light transport to examine potential errors with BOS and identify improvements which will allow the system to estimate optical grain size. We use a Monte Carlo radiative transfer model to estimate the influence of firn microstructure variations on borehole reflectance. We then use a ray-tracing algorithm to model the multiple reflections within the borehole that cause measured brightness variations. Multiple reflections cause the brightness measured at a point on the borehole wall to not necessarily be equal to the local wall reflectance. The ray tracing further shows that wall imperfections or variations in the camera position can produce brightness variations that are unrelated to changes in firn properties. Smooth walls and good stabilization of the camera help ensure that brightness variations result from variations in firn properties, and thus are a measure of firn stratigraphy, rather than artifacts.

## 1. INTRODUCTION

Firn processes are critical to a variety of glaciological problems. Calculations of an ice sheet's contribution to sea-level rise often use surface elevations to calculate the mass change, which requires an estimate of the density profile of the firn (e.g. Cuffey, 2008; Helsen and others, 2008; Pritchard and others, 2009). Accumulation rates are inferred by counting annual layers from polar firn cores (e.g. Kaspari and others, 2004) and are used to calibrate atmospheric circulation models (e.g. Van den Broeke and others, 2006). The timescales for paleoclimate records require an estimate of the age difference between the air trapped in bubbles and the ice enclosing it, which is a function of the time it takes for the firn to transform to ice (e.g. Schwander and others, 1997). The chemistry of the air trapped in the bubbles may also be affected by the structure of the firn (e.g. Dominé and Shepson, 2002). One factor limiting our understanding of firn processes is the difficulty in obtaining firn cores for detailed measurements. Borehole logging can help fill this information gap because it retains some of the detail of measurements made on cores but requires less labor as the core need not be recovered and transported.

Hawley and others (2003) used borehole video and a processing routine called borehole optical stratigraphy (BOS) to count annual layers and determine a depth–age scale that agreed well with optical and electrical techniques used on the recovered core. The wind-slab/depth-hoar couplet (Alley and others, 1997) is thought to cause the brightness variations, although the effect of variations in grain size or density is not well understood. Hawley and Morris (2006) measured density with a neutron density probe (Morris and Cooper, 2003) in the same borehole where BOS measurements were made. They found that brightness was strongly correlated with density at shallow

depths (upper 15 m), but that the correlation decreased with depth and became negative below 30 m. They interpreted the variation in correlation to be caused by a change in the densification regime at 15 m depth, but did not give a quantitative assessment of the importance of grain-size variations for the brightness signal.

Much theoretical work has been done on the interaction of electromagnetic radiation and snow grains (e.g. Warren, 1982), but research has focused on near-surface snow measured at flat air–snow surfaces, rather than on denser firn measured at curved borehole walls. Radiative transfer in boreholes requires more complicated modeling because borehole walls are curved and because photons may reflect off the borehole wall multiple times before they are detected at the camera. Modeling light transport in firn is also complicated by a lack of measurements to compare with theory. In this paper, we investigate how variations in firn properties produce measurable brightness variations with a pair of simplified models. We also examine how imperfections in the borehole wall and variations in the camera position may produce changes in wall brightness unrelated to changes in intrinsic firn properties.

## 2. MODELING

The path that light takes between the source and camera of a borehole video system can include multiple reflections from the borehole wall, and each reflection from the borehole wall can include multiple reflections from individual snow grains within the firn. Although it is possible to model both the multiple reflections from the wall and the multiple reflections from individual snow grains in one model, it is computationally expensive; the model would have to track millions of photons each time the camera and light source

were moved relative to features in the borehole. Instead, we divide the modeling into two parts: (1) propagation of photons through the firn and (2) multiple reflections of light from the borehole walls. We use a Monte Carlo, radiative transfer model to investigate how photons travel through the firn and to find the wall reflectance as a function of grain size and density. We use a ray-tracing algorithm to model the multiple reflections off the borehole wall and to investigate the effects of layering, wall imperfections and camera position on the brightness signal.

The goal of our modeling is to gain insight into the cause of brightness variations in borehole video logs. We simplify the modeling to focus only on changes in grain (or bubble) size and density. We do not attempt an exact solution of the radiative transfer equations. Assessing the effect of variations in grain shape on the brightness signal is difficult because relatively few observations of firn microstructure (e.g. Freitag and others, 2004; Baker and others, 2007; Hörhold and others, 2009) have been made at the level of detail required, and none have been linked with measurements of optical properties. Our simplified treatment allows a qualitative analysis of the cause of BOS brightness variations and potential errors associated with BOS logs. A full treatment of light propagation in firn is beyond the scope of this work.

## 2.1. Radiative transfer model of light transport in firn

### 2.1.1. Description of firn

Snow and firn have complex structures of interlocking grains of a variety of shapes and sizes (e.g. LaChapelle, 1992). At low densities ( $< \sim 550 \text{ kg m}^{-3}$ ), the firn can be considered a collection of snow grains in a matrix of air (e.g. Wiscombe and Warren, 1980; Warren and others, 2006), while at high densities ( $> \sim 800 \text{ kg m}^{-3}$ ) the firn is more like a collection of air bubbles in a matrix of ice (e.g. Mullen and Warren, 1988). In between is a transition region, where the difference between grains and bubbles becomes indistinct. The density and specific surface area (SSA), the area of the ice/air interface per unit volume, are two useful parameters for describing the complex structure of firn (e.g. Freitag and others, 2004). For modeling the optical properties of firn, we follow the widely applied assumption that the scattering and absorption properties of firn can be accurately represented by a collection of spheres with the same SSA and density (e.g. Wiscombe and Warren, 1980; Dozier and others, 1981; Mullen and Warren, 1988; Grenfell and Warren, 1999). The density and SSA uniquely determine an effective grain size and effective bubble size. Note that while the density and SSA are matched, the number of spheres is unlikely to equal either the number of snow grains or bubbles.

Dust, ash, soot and chemical impurities (e.g. sea salt) are also present in firn (e.g. Bertler and others, 2005). The dust and ash particles absorb visible light much more readily than ice and will cause a decrease in returned brightness in the firn (Warren and Wiscombe, 1980; Bay and others, 2001). In typical polar firn, the effects of dust, ash and impurities are small and the optical properties are dominated by scattering of light from ice/air boundaries (e.g. Bramall and others, 2005). Large concentrations of soot or other contaminants (e.g. a dense ash layer from a volcanic eruption) could dominate the microstructure-based effects we discuss here, but as these features are rarely found in firn in most parts of Greenland and Antarctica, we do not consider their effect.

### 2.1.2. Firn reflectance

We investigate the variations in firn reflectance for different combinations of density and either grain or bubble size with a Monte Carlo radiative transfer model. This model is better suited to our purposes than the adding-doubling (e.g. Hansen, 1971) and multi-stream methods (e.g. Bohren, 1987) used in other studies of ice surface albedo, because it allows treatment of a curved boundary and a point-like light source. The model determines the wall reflectance as a function of grain size, density and borehole radius. This model was adapted from a simple Monte Carlo code designed for analysis of radiation propagation in human tissue (Prah, 1988); the code will be available at: [http://gcmd.nasa.gov/getdif.htm?waddington\\_0335330](http://gcmd.nasa.gov/getdif.htm?waddington_0335330).

Our model tracks packets of photons that enter optically thick firn at a single location, simulating a collimated-beam light source. We assume no Fresnel reflection on the borehole wall. At each scattering event, a new direction for the packet is chosen from a Henyey–Greenstein (H-G) phase function (Henyey and Greenstein, 1941). The H-G phase function requires specification of the asymmetry parameter,  $g$ , the mean cosine of the phase angle of scattered photons. After several scattering events, the H-G phase function accurately approximates true phase functions with the same asymmetry parameter and allows high computational efficiency compared to calculations that use more detailed approximations of the phase function (e.g. Petty, 2006). A value of  $g=0$  yields isotropic scattering, while  $g=1$  yields pure forward scattering. Snow grains that are large compared to the wavelength of light are strongly forward-scattering, with  $g$  equal to  $\sim 0.89$  (Wiscombe and Warren, 1980); spherical air bubbles have  $g$  values between 0.85 and 0.86 (Mullen and Warren, 1988).

At the exit location, the contribution of each packet to the exit intensity is determined using an attenuation factor chosen depending on whether the modeled firn is most similar to a collection of ice grains in air or to a collection of air bubbles in ice:

$$dI(x, y, \theta, \omega, N) = \frac{I_0}{N_{\text{photons}}} \begin{cases} \omega^{N_{\text{scat}}} & \text{ice grains in air} \\ \exp(-k_{\text{ice}} L \frac{\rho_{\text{firn}}}{\rho_{\text{ice}}}) & \text{air bubbles in ice.} \end{cases} \quad (1)$$

Here  $x$  and  $y$  are Cartesian coordinates on the surface of the slab of firn,  $\theta$  is the angle at which the light exits the surface relative to the vertical axis,  $z$ ,  $I_0$  is the initial intensity and  $N_{\text{photons}}$  is the number of packets tracked. For ice grains in air, the absorption is determined by  $\omega$ , the single-scatter albedo for ice grains, and the number of scattering events,  $N_{\text{scat}}$ . For air bubbles in ice, the single-scattering albedo of the air bubbles is treated as unity, and the factor

$$\exp(-k_{\text{ice}} L (\rho_{\text{firn}} / \rho_{\text{ice}}))$$

accounts for absorption as a photon travels through the ice. Here  $k_{\text{ice}}$  is the absorption coefficient for ice (Warren and Brandt, 2008),  $\rho_{\text{firn}}$  and  $\rho_{\text{ice}}$  are the densities of the firn and ice, and  $L$  is the distance the photon traveled. The total absorption is assumed to be proportional to the volumetric ice concentration (Mullen and Warren, 1988). This process is repeated for  $\sim 10^7$  photons.

The outgoing intensity is in units of energy steradian $^{-1}$   $L_{\text{scat}}^{-2}$ . The scattering length,  $L_{\text{scat}}$ , is the e-folding distance for extinction of a photon along a

particular direction by scattering, and is found by

$$\frac{1}{L_{\text{scat}}} = \sigma_{\text{scat}} = n(r)\pi r^2 Q_{\text{scat}}, \quad (2)$$

where  $\sigma_{\text{scat}}$  is the scattering coefficient,  $n(r)$  is the density of scatterers per unit volume,  $r$  is the mean radius of the scattering particle and  $Q_{\text{scat}}$  is the scattering efficiency. The scattering efficiency gives the total scattering cross section for the particle per unit cross-sectional area; it depends on the wavelength of the radiation and the size and material properties of the particle. It is usually  $\sim 2$  because the path of a photon traveling near a snow grain or bubble can be deflected by diffraction.

The density of scatterers,  $n(r)$ , can be equated to mass density of the firn for grains in air,

$$\rho_{\text{firn}} = n(r_g) \frac{4}{3} \pi r_g^3 \rho_{\text{ice}}, \quad (3)$$

where  $r_g$  is the radius of the ice grains. For bubbles in ice,

$$\rho_{\text{firn}} = \rho_{\text{ice}} \left( 1 - n(r_b) \frac{4}{3} \pi r_b^3 \right), \quad (4)$$

where  $r_b$  is the radius of the bubbles. An equation for the scattering length as a function of grain size and density results from combining Equations (2) and (3) for grains in air:

$$L_{\text{scat}} = \frac{4}{3} \frac{\rho_{\text{ice}} r_g}{Q_{\text{scat}} \rho_{\text{firn}}}. \quad (5)$$

Combining Equations (2) and (4) for bubbles in ice,

$$L_{\text{scat}} = \frac{4}{3} \frac{\rho_{\text{ice}} r_b}{Q_{\text{scat}} (\rho_{\text{ice}} - \rho_{\text{firn}})}. \quad (6)$$

The model was designed to use units of the number of scattering lengths, so that the results from a single run can produce reflectances for different combinations of grain or bubble size and density. The only parameter of the firn that is specified in the Monte Carlo code is  $g$ . The output can be scaled to length units for any combination of grain or bubble size, density and scattering efficiency (appropriate values discussed below).

### 2.1.3. Applicability to wide density range

In our modeling results, we use parameters appropriate to scattering of light by large particles. The scattering efficiency is  $\sim 2$  for both ice grains in air (e.g. Warren and others, 2006) and air bubbles in ice (Fu and Sun, 2001). The single-scatter albedo for ice grains was calculated using

$$(1 - \omega) \approx 0.85 k_{\text{ice}} r_g \quad (7)$$

following Warren and others (2006). For air bubbles in ice, we assume there is no significant absorption during the scattering events ( $\omega = 1$ ) and account for absorption with the ice-path length factor in Equation (1). At transition densities, neither approximation is clearly more accurate than the other. For the large ice grains considered here, combining Equations (1), (5) and (7) gives the average absorption per scattering event as approximately  $1.28 k_{\text{ice}} \rho_{\text{firn}} / \rho_{\text{ice}}$ . By contrast, Equation (1) for bubbles in ice gives the average absorption per scattering event as  $\sim k_{\text{ice}} \rho_{\text{firn}} / \rho_{\text{ice}}$ , or about 30% less. The difference arises primarily because during a scattering event from an ice grain in air, photons take a complicated path that reflects multiple times off the air-ice interface, increasing the path length in the ice grain. Over the course of a particle's path through the firn, the larger asymmetry parameter for ice grains also tends to lead to

greater path lengths than those calculated for bubbles, leading again to more absorption.

The grains-in-air approximation has been validated against field measurements (e.g. Hudson and others, 2006) for densities smaller than the close-packed density. Theoretical arguments suggest this formulation should give reasonably accurate results for close-packed grains (Wiscombe and Warren, 1980). The bubbles-in-ice approximation matches measured reflectances for  $\rho_{\text{firn}} > 800 \text{ kg m}^{-3}$  (Mullen and Warren, 1988), but has not been tested at lower densities. We could transition smoothly between the two approximations by weighting each according to the density in the transition region. However, such an approach has two main problems: (1) we are aware of no measurements that indicate how the transition between the two approximations occurs, and (2) creating a smooth transition does not add insight into the processes causing variations in BOS brightness measurements. In the remainder of the paper, we show results from the grains-in-air approximation for all densities, and we present the results of the bubbles-in-ice approximation for  $\rho_{\text{firn}} > 550 \text{ kg m}^{-3}$  for comparison. Hereafter, we discuss the variations in firn microstructure in terms of density and grain size rather than bubble size.

### 2.1.4. Tracking the return of photons to boreholes

The cylindrical geometry of the borehole reduces the effective albedo of the wall; as the borehole radius decreases, photons become less likely to re-encounter the borehole during their random walk through the firn. To derive reflectances for a curved borehole wall, the Monte Carlo process is modified to give reflectances as a function of a scaled borehole radius,  $\Gamma$ , equal to the borehole radius divided by  $L_{\text{scat}}$ . In this model, the borehole axis runs parallel to the  $z$ -axis. The photons enter the borehole wall (at the origin of the coordinate system), traveling in the  $-x$  direction, and re-enter the borehole when  $(x - \Gamma)^2 + y^2 < \Gamma^2$ . The same photon may be tracked from a single starting position through several boreholes of different radius as long as the position, angle, distance traveled and number of scattering events is recorded the first time each photon re-enters a borehole of given diameter. The calculation is terminated when the photon re-enters the borehole with the smallest  $\Gamma$ , corresponding to the largest scattering length.

## 2.2. Ray-tracing model for multiple reflections in boreholes

### 2.2.1. Persistence of Vision ray-tracing algorithm

We use a ray-tracing algorithm to investigate how multiple reflections within the borehole produce variations in measured brightness. The ray-tracing package is the Persistence of Vision Raytracer (POV-Ray, <http://www.povray.org>). This has been used in a variety of research projects, including modeling radiant fluxes between building surfaces in urban environments (Lagouarde and others, 2010) and modeling light reflections in forest canopies (Casa and Jones, 2005). It tracks light rays from a source, through multiple reflections from objects with specified reflective properties, back to a camera. The light reaching the camera is calculated as a function of angle to produce an image. The modeled camera and light source were based on the GeoVision Jr<sup>TM</sup> borehole video camera used by Hawley and others (2003). The light source is a set of eight white light-emitting diodes (LEDs) forming a ring of 1.6 cm radius around the camera and angled out from the camera's optical axis by  $\sim 20^\circ$ . We verified that

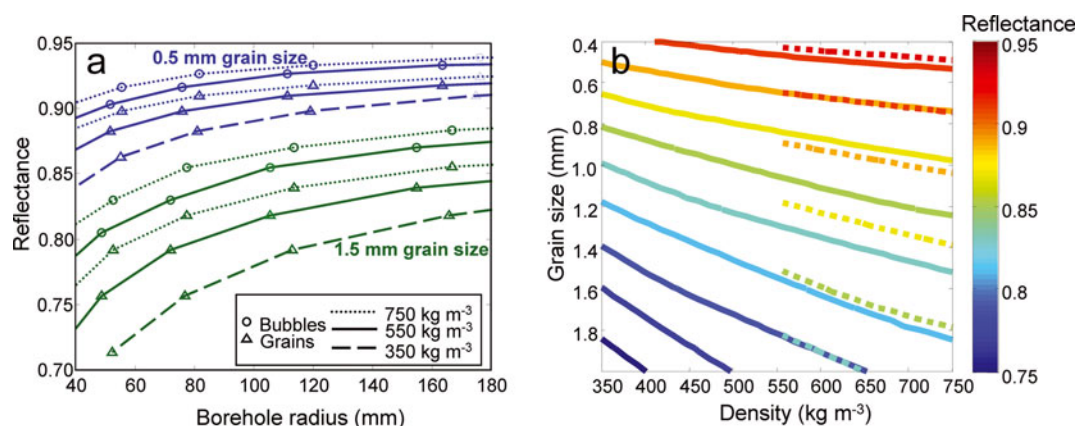


**Fig. 1.** The borehole wall reflectance depends on the grain size, density and borehole diameter. (a) Reflectance as a function of borehole radius for three different densities. For the two larger densities, the reflectance is calculated with the grains-in-air approximation (triangles) and the bubbles-in-ice approximation (circles). Grain sizes shown are 0.5 mm (blue) and 1.5 mm (green). (b) Reflectance for a 100 mm diameter borehole. The grains-in-air approximation is solid; bubbles-in-ice approximation is dashed. In both (a) and (b), the bubble size varies but matches the SSA and scattering length of the grain size and density combination.

the ray tracing reproduced the proper light emission, by simulating the illumination pattern of the model camera onto a diffuse, white surface and comparing the resulting images with the illumination pattern of the GeoVision Jr<sup>TM</sup> on a sheet of white paper. The borehole was modeled as a 10 cm diameter open cylinder, with the camera and light source at the center looking down the cylinder.

POV-Ray allows the user to specify both the fraction of light reflected and how that light is reflected from an object. Our choices for the fraction of light reflected from the borehole wall were guided by the radiative transfer results discussed below. We used a Lambertian reflectance model to describe the bidirectional reflectance function of the borehole wall. A Lambertian surface scatters light such that an observer perceives the same brightness from any viewing angle, and approximates our modeled surface well (see section 3.1.2). To model Lambertian reflectance, POV-Ray uses the Radiosity algorithm (Goral and others, 1984), in which surfaces are discretized into facets with Lambertian reflectance and the radiative transfer equation is solved to determine the radiant flux from each facet to each other facet.

### 3. RESULTS

#### 3.1. Radiative transfer model of light propagation in firn

##### 3.1.1. Borehole wall reflectance

Borehole wall reflectances are plotted as a function of grain size or bubble size for a series of borehole sizes in Figure 1a for three firn densities. The calculations were performed with an absorption coefficient of  $0.12 \text{ m}^{-1}$ , appropriate for light of 600 nm wavelength (Warren and Brandt, 2008). Decreasing the borehole radius decreases the reflectance because fewer photons find their way back into the borehole. This effect is shown schematically for ice grains in Figure 2a. The borehole reflectance is significantly greater for the bubbles-in-ice than the grains-in-air approximation. As discussed above, this is caused both by the lesser absorption per scattering event and by the shorter path lengths that result from the lower asymmetry parameter for bubbles,  $g=0.85$ , versus grains,  $g=0.89$ . The pattern of reflectance variation with borehole size is similar for the two approximations, but the difference

in magnitude between the two is greater than that caused by a shift in density of  $200 \text{ kg m}^{-3}$ . This suggests that the grain shape plays an important role in the brightness variations, which we have not modeled.

In Figure 1b, the reflectance is also seen to depend on the density and the grain size, both of which determine the

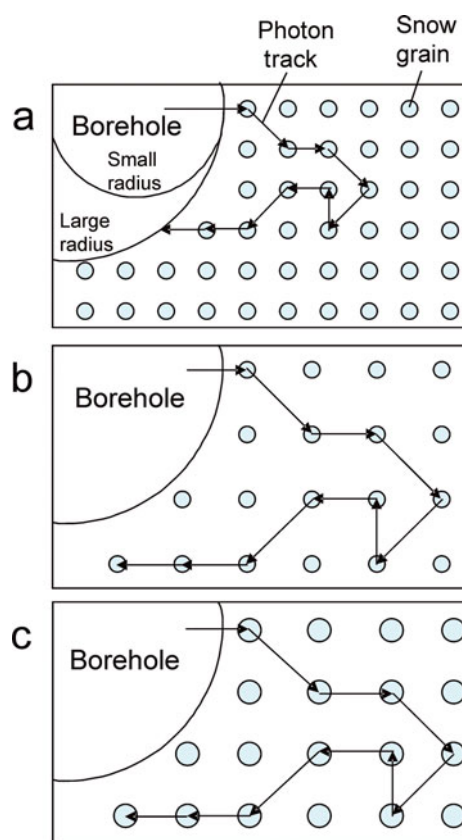


**Fig. 2.** Schematic showing the effects of varying the borehole radius (a), density (b) and grain size (c) on the likelihood of a photon returning to the borehole. Light-blue filled circles are snow grains. Arrows show photon paths. The photon scatters in the same direction at corresponding scattering events in each scenario. In (b) and (c) the photon does not return to the borehole because the scattering length has increased.

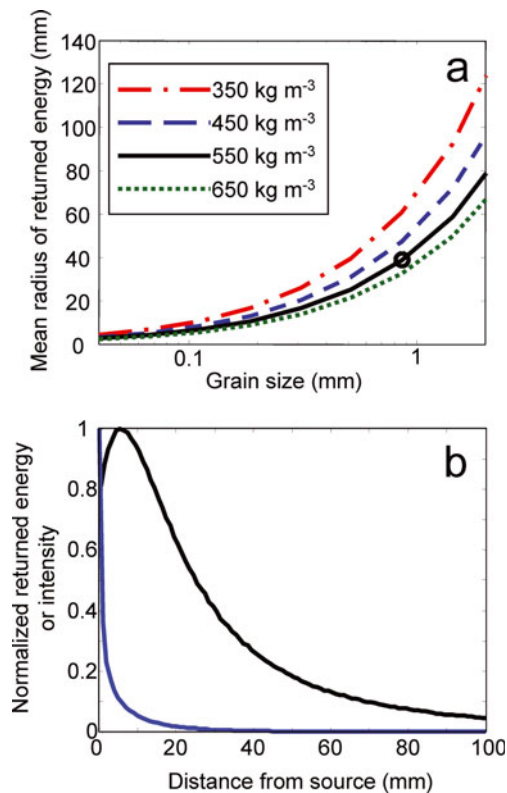


**Fig. 3.** (a) For a flat surface, the mean radius of returned energy can be calculated as the radius of the circle inside which half the energy exits the firn. It is defined in Equation (7). The circle marks the properties used in (b). (b) The fall-off of returned energy (black) and intensity (blue) with distance from the source for a flat wall and firn with a 1 mm scattering length. The returned energy is greater at 5 mm than at smaller radii because the percentage increase in area to which a photon returns increases faster than the fall-off in returned photons.

scattering length of the firn; fewer photons will return to the borehole for firn with a greater scattering length. Figure 2 shows how a photon that scatters in the same direction at each scattering event may not return to the borehole because of either an increase in grain size or a decrease in density. The decrease in reflectance from a decrease in density is due entirely to the change in scattering length, but an increase in grain size has a dual effect: a larger grain size both increases the scattering length and decreases the single-scatter albedo. Though variations in grain size change the borehole wall reflectance more than do variations in density, variations in either parameter can cause reflectance variations of the magnitude observed with BOS.

### 3.1.2. Distribution of light returned to the borehole

The radiative transfer model also determines the spatial displacement between the location at which photons enter the borehole wall in a single collimated beam and the location where they return. For high scattering lengths and/or high single-scatter albedos, the displacement can complicate small-field-of-view measurements of firn albedo and blur reflected-light imagery within boreholes. A simple way to describe the extent of spreading is the mean radius of returned energy,

$$\langle R \rangle = \frac{\int R I(R) dA}{\int I(R) dA}, \quad (8)$$

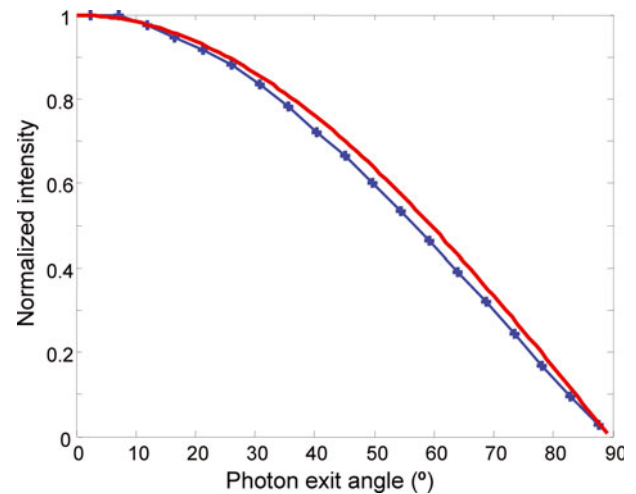


**Fig. 4.** Comparison of the intensity by exit angle for the radiative transfer model (blue with crosses) and the expected intensity for a Lambertian surface (red). A Lambertian surface has the same brightness from all viewing angles described by  $I(\theta) = I(0) \cos(\theta)$ , where  $I$  is intensity and  $\theta$  is the exit angle.

where  $R$  is the distance between the point where the photon enters and exits the firn. The mean radius of returned energy depends upon the grain size, density and asymmetry parameter. Figure 3a shows the displacement for different densities and grain sizes and an asymmetry parameter of 0.89. The returned energy in each increment of radius  $[R, R + dR]$  and the intensity for each increment of radius are shown as a function of radius (Fig. 3b). The intensity falls off more quickly than the returned energy because the area increases with increasing radius. The returned energy is greater at 5 mm than at smaller radii because the fractional area that a photon can return to increases rapidly at small radii and has a greater effect than the fall-off in returned photons with radius.

The intensity of the photons leaving the borehole wall as a function of angle relative to the wall normal,  $\theta$ , is shown in Figure 4. The normalized intensity curve matches the normalized curve for a Lambertian surface, for which  $I(\theta) = I(0) \cos(\theta)$ . The agreement is typically within a few percent, with a maximum difference of 15% at exit angles of  $\sim 75^\circ$ . The close agreement shows that it is appropriate to represent the borehole wall in the ray-tracing model as a Lambertian surface.

## 3.2. Ray-tracing model results of multiple reflections in boreholes

### 3.2.1. Simulations

We conducted two types of simulations: variations in the borehole wall and variations in the camera position or orientation. For variations in the borehole wall, we added a feature to the borehole: either a dark band for a change in firn properties, or an imperfection, a ridge or gouge, as might be produced during drilling. For each feature type, we simulated a BOS log by generating a series of frames in which the camera position varied from 1 m above to 1 m below the feature.

We reduced each of these frames to a single brightness value following the technique of Hawley and others (2003), averaging the pixels in a narrow annulus around the borehole for each frame to give the brightness for

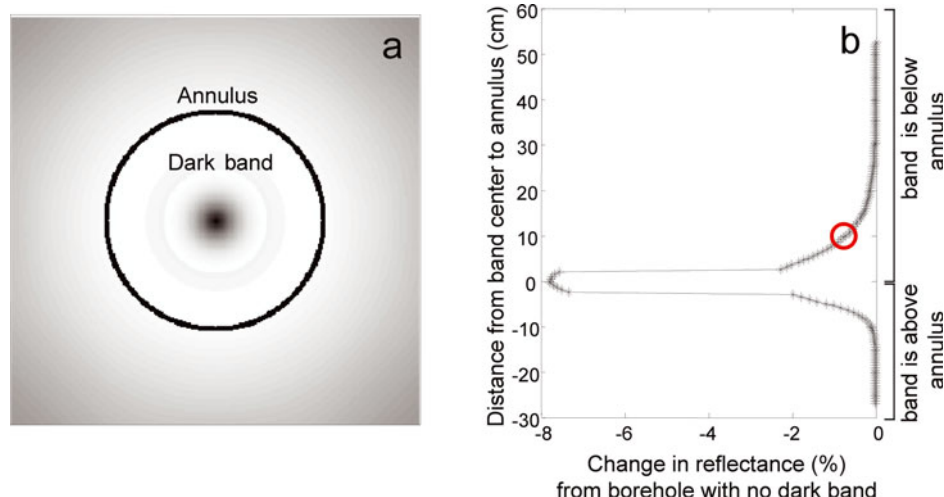


**Fig. 5.** (a) A borehole video frame created with the Persistence of Vision ray-tracing program. The annulus marks the pixels whose brightness values are averaged to create one brightness measurement. A band of lower reflectance is shown below the annulus. Wall reflectance is 80%, band reflectance is 5.26% less. (b) The percentage difference in brightness compared to a borehole with no dark band. Lowering the camera down a borehole is simulated by making a series of images (like (a)) as the feature is moved up the borehole relative to the camera. The red circle shows the brightness value from the image in (a).

$\sim 1$  vertical cm of the borehole wall. The annulus is located 10 cm below the camera (Fig. 5). All brightness logs are presented as the percentage change from the brightness in a borehole with the same wall reflectance but no feature. The y-axis has been re-centered such that 0 indicates when the center of the annulus is located on the center of a feature (Fig. 5b). This permits the change in recorded brightness with distance from the feature to be easily seen.

We also produced series of images that simulate the variations in the camera orientation and position that will occur if the stabilizers for the camera lose contact with the borehole wall. The camera can either point away from the borehole axis or move from the center of the borehole. In the first series of images, we varied the pointing angle of the camera from 0 to  $2.5^\circ$  from the borehole axis. In the second series of images, we moved the camera from the center of the borehole to 3 cm off-center. In both series, the borehole wall had a consistent reflectance for the entire depth.

### 3.2.2. Accounting for the spreading of light in firn

In the ray-tracing algorithm, the light rays reflect off the borehole wall at the location of impact; they do not spread through the firn. Even though some features (e.g. the ridges and gouges) are likely covered in drill dust (small snow grains produced by drilling) that makes the scattering length lower than that of the surrounding firn, the spreading of light will still be significant (Fig. 3a). To approximate the spreading of light, we convolved the brightness logs for the dark-band and ridge-and-gouge simulations with a 5 cm wide kernel based on the pattern of intensity found with the radiative transfer model for firn with a 1 mm scattering length (Fig. 3b). We performed a second convolution with a 5 cm Gaussian kernel to approximate the filtering done in post-processing (e.g. Hawley and others, 2003).

### 3.2.3. Band of lower reflectance

A layer in the firn with a different density and/or grain size than the local background norm was represented by a band of different reflectance. Dark bands of 5.26% less reflectance than the wall reflectance were modeled. The 5.26%

drop maintained consistency with the 95% background-reflectance case when the dark band was 90% reflective (5.26% is  $0.05/0.95$ ). The magnitude of the reflectance drop was based on reflectance changes of 1.5% and 3%, which we calculated from measurements of porosity and SSA for firn of depths 15 and 51 m from North Greenland (Freitag and others, 2004). The larger 5.26% drop helps reduce the numerical noise in the ray-tracing calculations. Simulations were run for three layer thicknesses, 2, 5 and 10 cm, and for two background borehole wall reflectances, 80% and 95%. The 95% simulations most closely resemble upper firn conditions of small grains and low scattering lengths. The 80% simulations are similar to deeper firn conditions, with larger grains and longer scattering lengths.

In all simulations, the drop in brightness measured at the band was greater than the 5.26% drop in reflectance of the band. Figure 6a shows the brightness variations for the three different bandwidths at 80% and 95% reflectance. The greater the borehole wall reflectance, the greater the fractional change in brightness at the center of the band. Furthermore, the decrease in brightness increased with the thickness of the band. The dark band also reduced the brightness beyond its edges: areas adjacent to the band, but above or below it, appeared darker, an effect that is more pronounced down-borehole from the dark band. The darkening occurs because the dark band absorbs some of the energy that is multiply reflected around the borehole. Having the dark band near the light source decreases the energy available to illuminate the borehole wall, and the brightness recorded at the annulus decreases, even if the annulus is not on the dark band.

The effects of light spreading through the firn and post-processing smoothing are shown in Figure 6b. The spreading of light decreases the magnitude of the brightness drop and smooths the measured signal at the band edge. The brightness change is reduced more for the thinner bands. The Gaussian smoothing has a similar effect, though the magnitude of the brightness drop at the center of the dark band is reduced more, particularly for the 2 cm thick bands.

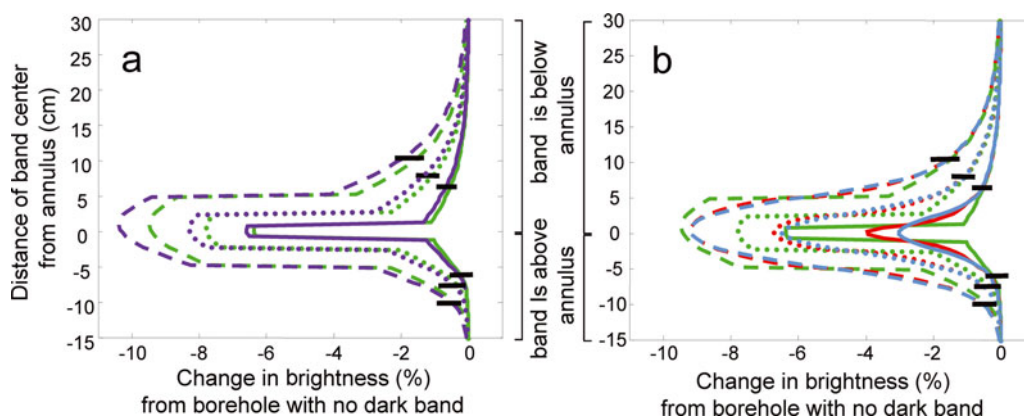


**Fig. 6.** Percentage decrease in brightness due to borehole-wall multiple reflection effects. Dark bands have widths of 10 cm (dashed), 5 cm (dotted) and 2 cm (solid) and 5.26% lower reflectance than the borehole wall. Horizontal lines indicate one borehole radius (5 cm) away from the edge of a dark band. (a) 80% (green) and 95% (purple) wall reflectance. (b) 80% wall reflectance in green is same as in (a). To approximate the spreading of light in firn, we convolve the brightness log with a 5 cm kernel based on the intensity fall-off from the radiative transfer modeling (red). To simulate post-processing smoothing, we convolve the brightness log with a 5 cm Gaussian kernel (light blue).

### 3.2.4. Ridges and gouges

Imperfections in the borehole wall are often formed when the drill is stopped to extend the drill stem length or to recover a core section. To simulate these imperfections, we generated a set of images, where either a ridge or a gouge was added to the borehole circumference (Fig. 7a and b). In a cross section along the length of the borehole, the ridge is a semicircular projection of radius 1 mm into the borehole; the gouge is a depression. The brightness log for a borehole with a ridge at 80% wall reflectance is shown in Figure 7c. The ridge causes a ring of high brightness and a smaller shadowed area below. The brightness is affected more below the ridge than above it; no effect of the ridge is noticeable one borehole radius (5 cm) away from the ridge in either direction. Simulations with a wall reflectance of 95% were similar, though the magnitude of the brightness variation was less because of the large amount of light already reaching the camera.

The simulation of a BOS measurement with a 1 mm gouge is shown in Figure 7d. As in the ridge case, both a ring of high brightness and a smaller shadowed area are created, but in this case the shadowed area is higher in the borehole. The brightness increase when the annulus is centered on the gouge is similar to that of the ridge. The brightness immediately above and below the gouge is decreased, but no effect is noticeable at distances of one borehole radius away.

The effect of light spreading in the firn and of smoothing in post-processing on these logs is shown in Figure 7e and f. The brightness peak of the ridge or gouge is substantially muted, but the brightness increase is spread over a larger vertical distance. The sharp drop in brightness is no longer observed. The brightness record becomes more similar to the brightness variations caused by variations in firn properties (Fig. 6b). Convolution of the brightness logs with the Gaussian kernel has a similar effect. The magnitude of the brightness signal is reduced but at the expense of making the signal from the wall imperfections visually more similar to a signal that might result from annual-scale layering.

### 3.2.5. Camera position and orientation

The effects of the camera pointing off the borehole axis and the camera pointing straight down but being offset from the

center of the borehole are shown in Figures 8 and 9. The brightness was calculated in two ways: (1) uncorrected – where, as above, the brightness was the average over an annulus of pixels 10 cm below the camera, centered on the middle of the image; and (2) corrected – where the annulus is re-centered on the darkest pixel in the image, which is a best guess of the bottom of the borehole. The brightness was also calculated for a half-annulus on each side of the borehole. The camera points (or is offset) toward the + side, and points (or is offset) away from the – side. For all images, the borehole wall reflectance was 80%.

As the camera tilt increases to  $2.5^\circ$ , the uncorrected half-annulus averages vary relative to the untilted image by up to 1.5% (Fig. 8). Correcting the averaging process by re-centering the annulus reduced this effect by about half. The uncorrected brightness variations of the two sides partly cancel each other for the full-annulus averages, but variations up to 0.5% can persist. Re-centering the annulus on the bottom of the borehole reduced the brightness variations to  $<0.2\%$ . Simulations with boreholes of 20% and 98% wall reflectance showed similar improvements.

The effect of the camera being offset from the center of the borehole is shown in Figure 9. The variations in brightness are significantly larger than in the tilted-camera case, with a drop in brightness for an offset of 3 cm as large as 35% for the whole annulus, and as large as 55% for the + side. Re-centering the annulus does little to reduce the change in brightness because the center of the borehole does not move significantly due to the camera displacement. A different correction is required for these errors. The smooth shape of the brightness-change vs offset curve allows us to calculate a correction as a function of two values that can be determined for any annulus on any video frame: the mean brightness for the annulus,  $B_0$ , and the difference between the maximum and minimum brightness on the annulus,  $\delta B$ . The corrected brightness,  $\hat{B}$ , can be found by

$$\hat{B} = B_0(1 + f(\delta B, B_0)). \quad (9)$$

If the correction were perfect, the corrected brightness would equal the brightness of the same annulus when the camera is centered in the borehole. We used a

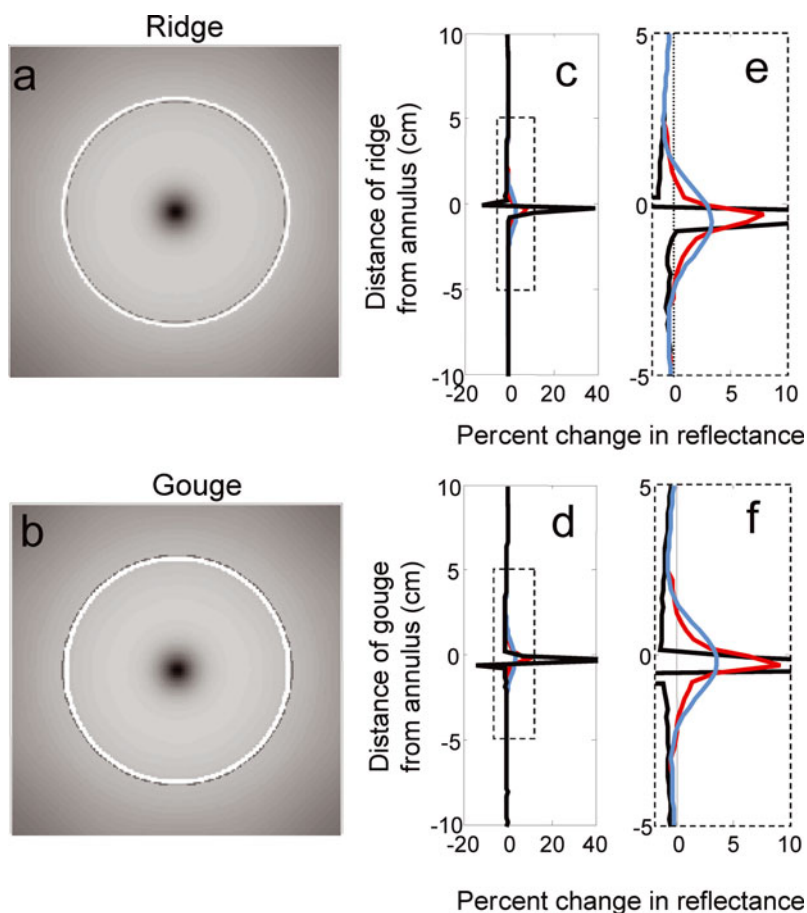


**Fig. 7.** Wall reflectance is 80%. (a) Ray-tracing image of borehole with a 1 mm ridge 10 cm below camera. Annulus is not shown. (b) Image of borehole with a 1 mm gouge 10 cm below camera. (c–f) Thick black curves show brightness change as camera is lowered past feature. The large (~40%) reflectance changes using ray tracing only are unrealistic because spreading of light in the firn is not incorporated in the ray-tracing model. To approximate the spreading of light, we convolve the brightness log with a 5 cm kernel based on the intensity fall-off from the radiative transfer modeling (red). To simulate post-processing smoothing, we convolve the brightness log with a 5 cm Gaussian kernel (light blue). Dashed boxes in (c) and (d) show area enlarged in (e) and (f).

second-degree polynomial for  $f$ ,

$$f(\delta B, B_0) = a \frac{\delta B}{B_0} + b \left( \frac{\delta B}{B_0} \right)^2, \quad (10)$$

and found the values for  $a$  and  $b$  that minimized the misfit between  $\hat{B}$  and the zero-offset brightness. A third-degree polynomial did not produce a noticeably better correction. For 80% wall reflectance and offsets less than 3 cm, the optimal coefficients were  $a=0.51$ ,  $b=0.3$ . This corrected the brightness to within 2.5% of the centered camera case. These same coefficients produced similar improvements for a wall reflectance of 98%. For a wall reflectance of 20%, the corrected brightness still varied from the camera-centered brightness by ~6%.

#### 4. DISCUSSION

BOS is an effective tool for identifying stratigraphic features in the firn. The features from one log can be used to count annual layers (Hawley and others, 2003), or repeat measurements (typically monthly or seasonally) in the same borehole can be used to measure vertical strain (R. Hawley and E. Waddington, unpublished information). The vertical strain measurements do not require a specific determination of the cause of the brightness features as long as the same

features can be identified in subsequent logs. However, the accuracy of the annual-layer count depends upon properly interpreting the brightness variations as seasonal changes in firn properties.

The two models described provide a framework for interpreting the brightness variations and understanding the limitations of borehole video. We focus our discussion on the accuracy of the annual-layer counts from BOS. We also include a short discussion of the limitations of borehole video on determining firn properties and suggest improvements for future devices.

##### 4.1. Effect on annual-layer counts

Accurate annual-layer counting with BOS requires that the brightness variations observed are caused by seasonal changes in the firn properties (e.g. grain size and density) and are not a result of either wall imperfections or variations in camera position. The ray-tracing calculations when corrected for spreading of light in the firn (Fig. 7) show that the brightness variations from wall imperfections are similar to variations caused by intrinsic firn properties. The brightness variations caused by wall imperfections could be incorrectly interpreted as annual layers. At Siple Dome, Antarctica, Hawley and others (2003) counted more layers in the upper 70 m than the visual and electrical methods used on the core. Some of the extra layers measured

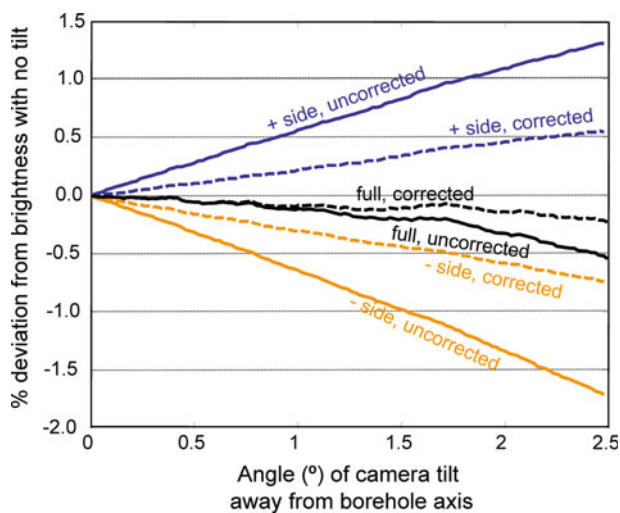


**Fig. 8.** Reflectance difference for the camera pointing off the borehole axis. Wall reflectance is 80%. Full annulus (black). The camera is pointing toward the + side (blue) and away from the – side (orange). Solid curves have no correction to the processing. Dashed curves improve the processing by re-centering on the darkest point in the image which is interpreted as the borehole center.

optically may have resulted from wall imperfections; the effects of wall imperfections are likely to be largest in the smaller-grained firn near the surface where volume scattering will be smallest. The best way to minimize the impact of wall imperfections on BOS logs is to use well-stabilized drills that leave the borehole with smooth walls. At Siple Dome, the borehole was drilled with a mechanically stabilized Eclipse drill, which produced relatively smooth walls, leading to a clean brightness log. When a hand-stabilized drill, a SideWinder, was used at the West Antarctic Ice Sheet Divide core site, the BOS brightness logs were difficult to interpret, likely due to scarring on the borehole wall (unpublished results).

Camera stabilization is also important for high-quality BOS logs. Variations in the camera angle and position can produce features that could be identified as part of the annual signal. These features can be identified and corrected if they come from angular misalignment between the camera and the borehole. However, it is difficult to identify and correct the log if the camera moves from the center of the borehole. A partial correction is possible based on the maximum, minimum and mean brightness for the annulus. However, this relationship is most accurate for a wall reflectance of 80%, and can over- or under-correct if the reflectance is significantly less.

Hawley and others (2003) calculated the brightness for each quarter of the borehole and found the same pattern of brightness variations for all quarters. They interpreted this to indicate they were seeing near-horizontal layers. This test is also important for checking the stabilization of the camera. Camera-position errors will result in non-synchronous brightness variations on different parts of the borehole wall. The absence of brightness variations between sections of the borehole supports the interpretation that the brightness variations are caused by firn properties.

The good agreement of the annual-layer counts from BOS, optical stratigraphy and electrical stratigraphy (Hawley and others, 2003) suggests that wall imperfections and

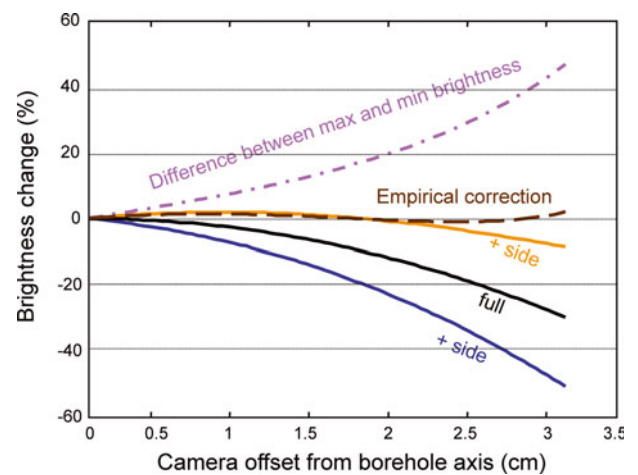


**Fig. 9.** Brightness change between a camera offset in the borehole and one centered. The camera is offset toward the + side (blue) and away from the – side (orange). The empirical correction (brown dashed) uses the full annulus brightness and the difference between the maximum and minimum brightness (purple dash dot) of the annulus to find the best estimate of what the brightness would be if the camera were centered in the borehole. See text and Equations (9) and (10) for description of empirical correction.

camera-pointing errors were not a major source of uncertainty at Siple Dome. Our modeling shows that BOS observations are most accurate when the borehole was drilled with a mechanically stabilized drill that limits wall imperfections and has a constant diameter that allows good stabilization of the camera.

#### 4.2. Limitations of BOS and suggestions for future devices

An objective of borehole measurements is the quantitative determination of physical properties of the firn. While BOS is effective at identifying stratigraphic markers in the firn, it is ill-suited for recovering firn properties. Since BOS makes only one measurement of brightness integrated over the visible spectrum, it is not surprising that it cannot distinguish between grain-size and density variations as the cause of the brightness variations. There are additional limitations as well. The ray-tracing results demonstrate that BOS does not measure the local wall reflectance but rather some nonlinear average of the wall reflectances near the point of measurement. The complex viewing geometry that comes from a downward-looking camera is unnecessary; a device with a single light source (e.g. an LED) and a detector (e.g. a photodiode) can measure the local wall reflectance because the influence of multiple reflections will largely be eliminated.

Another limitation of the current BOS configuration for inferring firn properties is that it operates in the visible spectrum. The brightness variations are sensitive to changes in both grain size and density as shown with the radiative transfer modeling (Fig. 1). Even if the BOS measurements are paired with a log of density, such as from a neutron density probe (Morris and Cooper, 2003), it is unlikely that BOS can provide much information about the grain size or SSA of the firn. In the radiative transfer results, the difference in reflectance depending on whether the firn is treated as ice grains in air or air bubbles in ice also shows that the reflectance is sensitive to grain shape. Because ice

is weakly absorbing in the visible spectrum, photons can scatter many times without being absorbed and the energy returned to the borehole is sensitive to the degree of forward scattering. In the near infrared, ice is much more strongly absorbing, and the absorption predominantly determines the energy returned to the borehole. A device using a near-infrared wavelength may be more effective at quantitatively estimating the grain size or SSA of the firn (e.g. Matzl and Schneebeli, 2006).

## 5. CONCLUSION

Two models were used to examine how light emitted from a borehole video camera interacts with firn. A radiative transfer model, treating the firn as a collection of ice grains in air, showed that changes in borehole reflectance could be caused by variations in either density or grain size; photons are less likely to return when the scattering length (a function of both grain size and density) is large. Multiple combinations of grain size and density can produce the same wall reflectance, so BOS, making only a single measure of brightness in the visible spectrum, cannot distinguish between variations in firn density and grain size.

Ray-tracing modeling showed the importance of the multiple reflections from the borehole wall before photons return to the camera. Those multiple reflections cause the observed brightness to be a nonlinear average of the borehole-wall reflectance approximately one borehole diameter above and below the point of measurement. Imperfections on the borehole wall and non-centered camera positions can produce brightness variations that are unrelated to changes in firn properties. Smooth borehole walls and a well-stabilized camera improve the BOS brightness logs, yielding accurate annual-layer counts.

## ACKNOWLEDGEMENTS

We thank E. Waddington for many productive conversations, comments on drafts, and consistent support for this work. We also thank R. Hawley for ideas and suggestions. We appreciate funding from the US National Science Foundation Office of Polar Programs grants 0335330, 0538639 and 0352584. The comments of E. Morris, an anonymous reviewer and the Scientific Editor, J. Glen, greatly improved the manuscript.

## REFERENCES

- Alley, R.B. and 11 others. 1997. Visual-stratigraphic dating of the GISP2 ice core: basis, reproducibility, and application. *J. Geophys. Res.*, **102**(C12), 26,367–26,382.
- Baker, I., R. Obbard, D. Iliescu and D. Meese. 2007. Microstructural characterization of firn. *Hydrol. Process.*, **21**(12), 1624–1629.
- Bay, R., P. Price, G. Clow and A. Gow. 2001. Climate logging with a new rapid optical technique at Siple Dome. *Geophys. Res. Lett.*, **28**(24), 4635–4638.
- Bertler, N.A.N. and 53 others. 2005. Snow chemistry across Antarctica. *Ann. Glaciol.*, **41**, 167–179.
- Bohren, C.F. 1987. Multiple scattering of light and some of its observable consequences. *Am. J. Phys.*, **55**(6), 524–533.
- Bramall, N.E., R.C. Bay, K. Woschnagg, R.A. Rohde and P.B. Price. 2005. A deep high-resolution optical log of dust, ash, and stratigraphy in South Pole glacial ice. *Geophys. Res. Lett.*, **32**(21), L21815. (10.1029/2005GL024236.)
- Casa, R. and H.G. Jones. 2005. LAI retrieval from multiangular image classification and inversion of a ray tracing model. *Remote Sens. Environ.*, **98**(4), 414–428.
- Cuffey, K.M. 2008. Climate change: a matter of firn. *Science*, **320**(5883), 1596–1597.
- Dominé, F. and P.B. Shepson. 2002. Air–snow interactions and atmospheric chemistry. *Science*, **297**(5586), 1506–1510.
- Dozier, J., S.R. Schneider and D.F. McGinnis, Jr. 1981. Effect of grain size and snowpack water equivalence on visible and near-infrared satellite observations of snow. *Water Resour. Res.*, **17**(4), 1213–1221.
- Freitag, J., F. Wilhelms and S. Kipfstuhl. 2004. Microstructure-dependent densification of polar firn derived from X-ray microtomography. *J. Glaciol.*, **50**(169), 243–250.
- Fu, Q. and W. Sun. 2001. Mie theory for light scattering by a spherical particle in an absorbing medium. *Appl. Opt.*, **40**(9), 1354–1361.
- Goral, C.M., K.E. Torrance, D.P. Greenberg and B. Battaile. 1984. Modeling the interaction of light between diffuse surfaces. *Comput. Graph.*, **18**(3), 213–222.
- Grenfell, T.C. and S.G. Warren. 1999. Representation of a nonspherical ice particle by a collection of independent spheres for scattering and absorption of radiation. *J. Geophys. Res.*, **104**(D24), 31,697–31,709.
- Hansen, J.E. 1971. Multiple scattering of polarized light in planetary atmospheres. Part I. The doubling method. *J. Atmos. Sci.*, **28**(1), 120–125.
- Hawley, R.L. and E.M. Morris. 2006. Borehole optical stratigraphy and neutron-scattering density measurements at Summit, Greenland. *J. Glaciol.*, **52**(179), 491–496.
- Hawley, R.L., E.D. Waddington, R.A. Alley and K.C. Taylor. 2003. Annual layers in polar firn detected by borehole optical stratigraphy. *Geophys. Res. Lett.*, **30**(15), 1788. (10.1029/2003GL017675.)
- Hawley, R.L., E.M. Morris and J.R. McConnell. 2008. Rapid techniques for determining annual accumulation applied at Summit, Greenland. *J. Glaciol.*, **54**(188), 839–845. (10.3189/002214308787779951.)
- Helsen, M.M. and 7 others. 2008. Elevation changes in Antarctica mainly determined by accumulation variability. *Science*, **320**(5883), 1626–1629.
- Heney, L.C. and J.L. Greenstein. 1941. Diffuse radiation in the galaxy. *J. Astrophys.*, **93**, 70–83.
- Hörhold, M.W., M.R. Albert and J. Freitag. 2009. The impact of accumulation rate on anisotropy and air permeability of polar firn at a high-accumulation site. *J. Glaciol.*, **55**(192), 625–630.
- Hudson, S.R., S.G. Warren, R.E. Brandt, T.C. Grenfell and D. Six. 2006. Spectral bidirectional reflectance of Antarctic snow: measurements and parameterization. *J. Geophys. Res.*, **111**(D18), D18106. (10.1029/2006JD007290.)
- Kaspari, S. and 6 others. 2004. Climate variability in West Antarctica derived from annual accumulation-rate records from ITASE firn/ice cores. *Ann. Glaciol.*, **39**, 585–594.
- LaChapelle, E.R. 1992. *Field guide to snow crystals*. Cambridge, International Glaciological Society.
- Lagouarde, J.-P. and 6 others. 2010. Modelling daytime thermal infrared directional anisotropy over Toulouse city centre. *Remote Sens. Environ.*, **114**(1), 87–105.
- Matzl, M. and M. Schneebeli. 2006. Measuring specific surface area of snow by near-infrared photography. *J. Glaciol.*, **52**(179), 558–564.
- Morris, E.M. and J.D. Cooper. 2003. Density measurements in ice boreholes using neutron scattering. *J. Glaciol.*, **49**(167), 599–604.
- Mullen, P.E. and S.G. Warren. 1988. Theory of the optical properties of lake ice. *J. Geophys. Res.*, **93**(D7), 8403–8414.
- Petty, G.W. 2006. *A first course in atmospheric physics. Second edition*. Madison, WI, Sundog Publishing.
- Prahl, S.A. 1988. Light transport in tissue. (PhD thesis, University of Texas, Austin.)

- Pritchard, H.D., R.J. Arthern, D.G. Vaughan and L.A. Edwards. 2009. Extensive dynamic thinning on the margins of the Greenland and Antarctic ice sheets. *Nature*, **461**(7266), 971–975.
- Schwander, J., T. Sowers, J.M. Barnola, T. Blunier, A. Fuchs and B. Malaizé. 1997. Age scale of the air in the Summit ice: implication for glacial–interglacial temperature change. *J. Geophys. Res.*, **102**(D16), 19,483–19,493.
- Van den Broeke, M., W.J. van de Berg and E. van Meijgaard. 2006. Snowfall in coastal West Antarctica much greater than previously assumed. *Geophys. Res. Lett.*, **33**(2), L02505. (10.1029/2005GL025239.)
- Warren, S.G. 1982. Optical properties of snow. *Rev. Geophys.*, **20**(1), 67–89.
- Warren, S.G. and R.E. Brandt. 2008. Optical constants of ice from the ultraviolet to the microwave: a revised compilation. *J. Geophys. Res.*, **113**(D14), D14220. (10.1029/2007JD009744.)
- Warren and W.J. Wiscombe. 1980. A model for the spectral albedo of snow. II. Snow containing atmospheric aerosols. *J. Atmos. Sci.*, **37**(12), 2734–2745.
- Warren, S.G., R.E. Brandt and T.C. Grenfell. 2006. Visible and near-ultraviolet absorption spectrum of ice from transmission of solar radiation into snow. *Appl. Opt.*, **45**(21), 5320–5334.
- Wiscombe, W.J. and S.G. Warren. 1980. A model for the spectral albedo of snow. I. Pure snow. *J. Atmos. Sci.*, **37**(12), 2712–2733.

*MS received 8 March 2010 and accepted in revised form 12 June 2010*